Cassini plasma spectrometer thermal ion measurements in Saturn's inner magnetosphere

R. J. Wilson,[1] R. L. Tokar,[1] M. G. Henderson,[1] T. W. Hill,[2] M. F. Thomsen,[1] and D. H. Pontius Jr.[3]

[1] Plasma data from the Cassini Plasma Spectrometer experiment are analyzed using a robust forward modeling technique for dayside equatorial orbits within the range 5.5 to 11 Saturn radii (1 R_S = 60,268 km). It is assumed the measured ion data may be represented by two anisotropic Maxwellian distributed species, H^+ and a water group ion, W^+. Saturn's magnetospheric plasma is shown to subcorotate by $15-30\%$ below rigid corotation within this region, with a minimum in fractional lag between 7 and 9 R_S. There is a suggestion of a small radial outflow, but the selection of data for this study precluded the inclusion of interchange injection events. Ion densities are in excellent agreement with the Cassini plasma wave instrument, giving confidence in the forward modeling technique. Plasma moments including density, temperatures, and velocities are presented, along with empirical models for density and azimuthal velocity. Water group temperature anisotropies $T_\perp/T_\parallel$ have values between 3 and 8 near 5.5 R_S, becoming less anisotropic as distance increases, but are still not isotropic by 10 R_S. The implications of these results for mass loading in the Saturnian magnetosphere are discussed, with the conclusion that an important fraction of the plasma source is located inside of the 5.5 R_S boundary of this study.

1. Introduction

[2] Pioneer 11 first flew by Saturn in 1979, followed by Voyager 1 in 1980 and Voyager 2 in 1981. *Wolfe et al.* [1980] used the plasma analyzer aboard Pioneer 11 to investigate Saturn's plasma environment, within the energy range of 100 to 18000 eV. They reported that the proton bulk speeds were below the energy range of the instrument. They assumed corotation of isotropic Maxwellian distributions in order to determine the mass/charge ratio of the incident ions, and discovered that attributing the ions to O^+ rather than H^+ provided a far better fit to the data. The Voyager spacecraft provided two further flybys, neither equatorial, with ion plasma instruments that covered an energy-per-charge range of 10 to 5950 V over 16 contiguous bins. By assuming isotropic Maxwellians, *Richardson* [1986] reported that plasma was at rigid corotation at distances inside L = 5.5 and L = 7 for the Voyager 1 and 2 flybys, respectively, and that the moons Dione and Rhea

were local plasma sources (L = equatorial distance in units of R_S).

[3] In 2004 Cassini arrived at Saturn and became the first orbiter, allowing far greater coverage of the Saturnian magnetosphere over a variety of radial distances, local times and latitudes. The Cassini Plasma Spectrometer (CAPS) [*Young et al.*, 2004] has a larger energy range and greater angular sampling than previous detectors at Saturn. This data set is utilized here to investigate positive ion velocity moments at equatorial latitudes, including densities, temperatures, and temperature anisotropies of both light and heavy ions and their common bulk flow velocities. The results are compared to previous mission results and those of complementary Cassini instruments, and their implications for plasma sources and transport are briefly discussed.

2. Instrument and Data Set

[4] The Ion Mass Spectrometer (IMS) sensor is a component of CAPS. CAPS produces a variety of data products, including singles data (E/q only) and time-of-flight data (E/q with time of flight allowing determination of m/q of detected ions). Ions pass through a top-hat analyzer held at a constant voltage bias to select ions in a particular range of kinetic energy-to-charge ratio, with energy resolution $(\Delta E/E)_{FWHM} = 0.17$. An ion of the correct ratio then passes through a carbon foil and knocks out electrons to create a signal at the start anodes. Ions continue on to stop anodes, and the time

---

[1]Space and Atmospheric Sciences Group, Los Alamos National Laboratory, Los Alamos, New Mexico, USA.
[2]Department of Physics and Astronomy, Rice University, Houston, Texas, USA.
[3]Physics Department, Birmingham-Southern College, Birmingham, Alabama, USA.
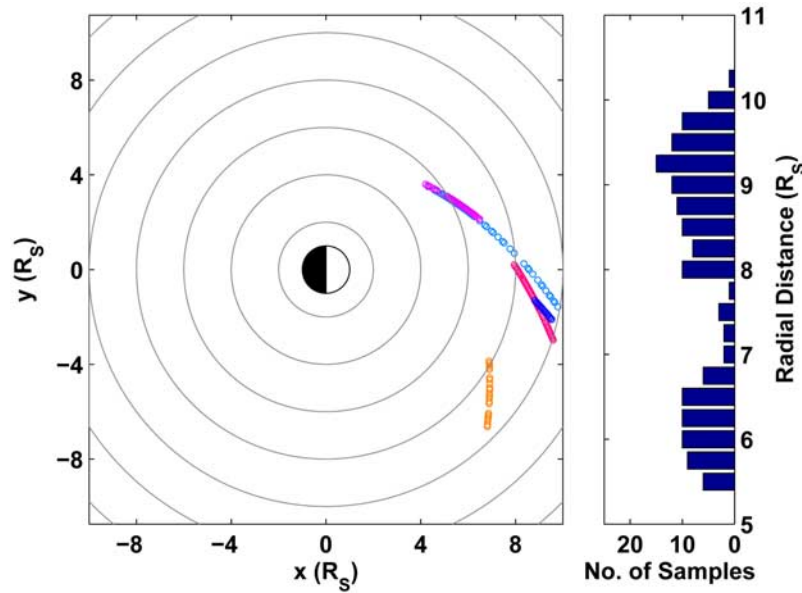
Figure 1. (left) A plot showing the location of the 150 suitable intervals used in this study for moments forward modeling. X and Y are in the equatorial plane with X pointing toward the Sun, while the different colors represent the different orbits. No Z coordinate is shown as all data points are within ±0.4° latitude of the equator. (right) The distribution of these intervals as a function of radial distance.

between the start and stop signals, combined with knowledge of the energy-to-charge ratio, allows a determination of the mass per charge of the ion. The IMS top-hat analyzer cycles through 63 logarithmically spaced voltage levels every 4 seconds in order to measure incident ions of 1 eV/e to 50 keV/e.

[5] In Saturn's magnetosphere the time-of-flight analysis often requires long integration times to build up enough statistics to categorize ions. The singles data product is the number of incident ions counted by the start anodes. Since it does not require a corresponding stop signal, it has a significantly higher efficiency than the time-of-flight measurements. The disadvantage is that while the incident ion's energy-to-charge ratio is known, its mass or charge state is not, but the advantage is that the singles data are taken at 4-s time resolution and are often statistically significant. Depending on the telemetry mode of Cassini, this data set may be down-linked as a single record of 63 values, or may have 2, 4 or 8 records summed together, giving a time resolution of 4, 8, 16 or 32 s.

[6] Because Cassini is a 3-axis stabilized craft, an actuator is employed to rotate the CAPS instrument to provide up to 208 degrees of viewing about the main spacecraft axis (azimuth), or it may be fixed at a particular orientation [*Young et al.*, 2004]. However, because different Cassini instruments have different pointing requirements, CAPS is not always pointing in an ideal direction, even with the use of the actuator. The 8 IMS start anodes are each 20 degrees wide, giving a field of view of ±80 degrees in the polar direction of the spacecraft. For a given detected ion, the start anode and the position of the actuator determine the direction of the incident ion.

3. Orbits and Initial Data Selection

[7] This study addresses the region of the inner magnetosphere between 5.5 and 11 R_s from Saturn's center (1 R_s = 60268 km = Saturn's radius). Cassini trajectories near Saturn's equatorial plane were desired to avoid complications of data sampled from varying latitudes. It was also important that the IMS instrument be able to view the corotating plasma, so only intervals when the actuator was in use and sweeping through the corotation direction were considered. A further criterion on the actuation required that individual IMS anodes should view a range of pitch angles in one actuation cycle rather than being fixed at the same pitch angle (an initial contingency for potential variances in inter-anode calibrations that was later found to be unnecessary). Intervals with close flybys of moons were rejected as the moon's proximity could perturb the results. Finally, distances less than 5.5 R_s were rejected because pickup ion populations are believed to be significant there, with the consequence that their distributions in singles data overlap those of the core populations. Analysis of these pickup ion distributions is the subject of a separate study [*Tokar et al.*, 2008].

[8] A survey of data between 2005 and mid-2006 (the equatorial orbits) highlighted five potential Cassini trajectory segments through the inner magnetosphere. These occurred on the following days: 11 October 2005, 27 November 2005, 24 December 2005, 24/25 February 2006, and 28 April 2006. Figure 1 shows the intervals that were used in the study. Local times range from 9 to 15 hours and radial distances from 5.5 to 11 R_s, with a few trajectory segments being very similar. Saturn Orbit Insertion (SOI) was not considered because the actuator was in a fixed position throughout, leading to poor phase space sampling, and because the trajectory was several degrees off the equatorial plane.

4. Data Analysis

[9] Usually plasma instruments are on a spinning spacecraft, allowing sampling over a full 4π steradians so that
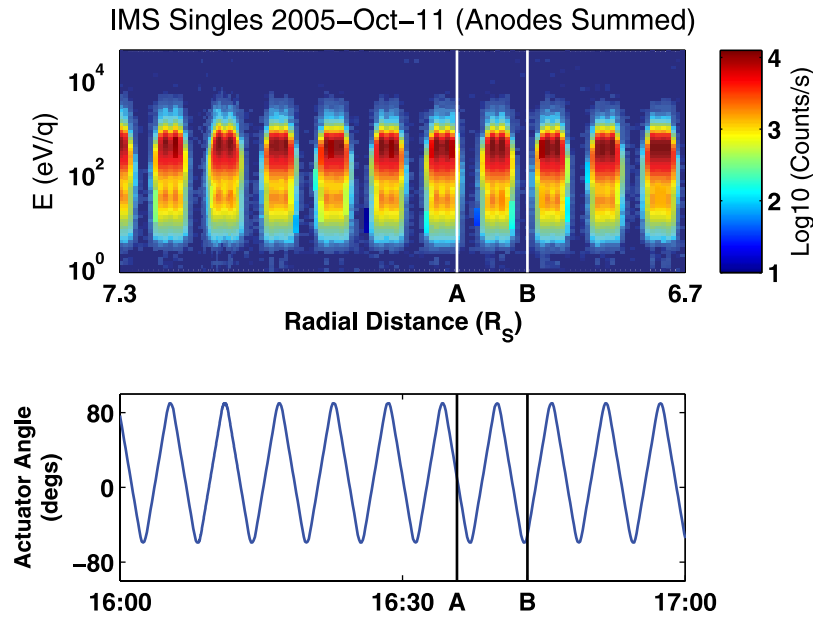
Figure 2. (top) An example spectrogram of IMS singles data, found by summing the 8 individual anodes together and shown on a log scale. The vertical axis is energy per charge of incident ions, while the horizontal is time; the corresponding radial distances from Saturn are indicated below the spectrogram. (bottom) The actuator angle for the same period of time. For this example, IMS observes the peak flow when the actuator is at $\approx70°$. Since the upper actuator limit is $\approx90°$, the actuator passes through the peak flow twice per actuation cycle. This can be seen in the spectrogram as pairs of peaks. When IMS looks away from the peak flow (i.e., $\approx-60°$), the measured count rate plummets to negligible values, highlighting the requirement of being able to view the peak flow in order to have data with enough counts to analyze. The interval A-B is investigated further in Figures 3 and 4 and is of the duration required for one moments calculation.

straightforward numerical integration can be used to compute velocity moments. The challenge of numerically integrating the singles data is the problem of partitioning the counts at any given energy level to the different species. If the partition is not correct, different species can show different flow velocities perpendicular to **B**, which is an unphysical result. Additionally, since CAPS can only view a maximum of 208 out of 360 degrees in azimuth, other techniques for generating moments must be employed. For example, *Thomsen and Delapp* [2005] and *Sittler et al.* [2005] used a method that utilizes direct integration of available counts and looks for symmetry within the distribution. In this study we calculate ion moments by forward modeling of IMS data, a technique used by *Young et al.* [2005] and *Tokar et al.* [2005] to identify O_2^+ near Saturn's rings and by *Tokar et al.* [2006] to analyze CAPS data near the moon Enceladus. The forward modeling requires that all species have the same bulk flow velocity but the ion composition, densities and temperatures are free parameters to be determined by the best match to the observed total ion (singles) measurements. In this paper we employ optimization algorithms in the forward modeling procedure.

[10] From IMS time-of-flight data it is known that ions in the inner magnetosphere are dominated by a water group and a lesser light ion group [*Young et al.*, 2005; *Sittler et al.*, 2005]. The water group, W^+, consists of O^+, OH^+, H_2O^+ or H_3O^+ ions, and the light ions are H^+. The model assumes two populations, one with m/q = 1 amu/e and one with

m/q = 17 amu/e. Tests show that assuming a different water group ion, or simply an equal density of all four W^+ ions, resulted in little difference to the final moments modeled. On one such test at 6 R_S over a range of masses from 16 to 19 amu the densities are within 14% while temperatures and velocities are both within 9%. Figure 2 shows a spectrogram of singles data, where the dominant water group can be seen at ~500 eV/q, and the light ion group at ~40 eV/q.

[11] In the forward modeling code, the two ion species are modeled as anisotropic Maxwellian distributions, with both species having the same bulk flow. This gives 9 free parameters for the code to fit; n^W, $T_\perp^W$, $T_\parallel^W$, n^H, $T_\perp^H$, $T_\parallel^H$, V_ρ, V_φ and V_z, where n is density, $T_\perp$ and $T_\parallel$ are perpendicular and parallel temperatures and V is velocity in cylindrical coordinates aligned with Saturn's spin axis. Since the Cassini orbits used here are very close to the equatorial plane, the magnetic field direction is assumed to be anti-parallel to Saturn's spin axis in order to speed up computation. Kappa distributions have also been investigated, with the kappa parameter for each ion species being another free parameter in the fit. However, this drastically increased computation time, gave distributions with large kappa values that were essentially Maxwellian, and did not improve the fits.

[12] Simulated ion counting rate distributions versus E/q are then calculated on the basis of spacecraft pointing and the actuator's position at any given time. Instrument effects

are also included in the model, such as anode cross talk where a fraction of ions incident on a look direction of a particular anode are counted in neighboring anodes instead (see *Thomsen and Delapp* [2005] for further details; this report is available at http://nis-www.lanl.gov/nis-projects/caps/Moments_Computation.pdf). Spacecraft potential was not accounted for; however, this should not have a significant effect on the dominant water group whose distributions are peaked above 100 eV. The background count rate due to penetrating radiation (which also shows a dependence on actuator angle) is estimated from the measured data and also accounted for within the simulated distributions. The background algorithm used is applied to each anode individually and considers data summed to 32-s segments, where the background for that interval is defined as the value that 95% of the energy bins counts (at all energies below 25 keV) are above. In practice, for the 59 bins below 25 keV this means that the second lowest count value observed is used as the background value for that anode for that interval.

[13] For each moments calculation it is desired to sample as much of phase space as possible, hence a complete actuation cycle is required. A 448 s duration is used (14 × 32-s data samples), which is just over a full actuator cycle (the actuator motion is not synchronous with the singles data sampling) and also is suitable for use with all telemetry modes.

[14] The simulated ion counting rates across all 8 anodes for all data records within this 448 s interval are then compared against the measured IMS singles data using a statistical cost function. The cost function is a scalar value calculated as the sum of (observed counts − simulated counts)^2/(observed counts + 1) for each data sample, anode and energy bin within the interval, plus any penalty values (various multiples of 10^{10}) incurred should one of the free parameters violate a constraint. The 9 free parameters are varied randomly and a new simulated ion counting rate distribution is generated and compared against the measured IMS singles data. This process is repeated tens of thousands of times until the best fitting densities, temperatures and velocities are identified as the set of parameters that gave the minimum cost function.

[15] The minimization of the cost function is performed sequentially using three different optimizers, Adaptive Simulated Annealing (ASA) [*Ingber*, 1993a, 1993b, 1996], Simplex [*Press et al.*, 1992] and Praxis [*Brent*, 1973; *Powell*, 1964] routines, in order to sample all parameter space to identify the global minimum rather than a local one. ASA is utilized to find a good approximation to the global minimum quickly, but is slow to converge on the solution so after 20,000 cycles it terminates (previous testing had shown just 2,000 cycles were required to find a good approximation to the minimum). The Simplex and Praxis routines then use the good approximation from ASA to calculate the actual minimum value. Constraints, in the form of sliding penalty functions, are included within the fitting routines by placing upper and lower limits on each free parameter, to avoid wasting computational time on unphysical situations, such as negative density or temperatures (i.e., if a n^W of -3 cm^{-3} is attempted a penalty of $+3.10^{10}$ is added to the cost function value). Another constraint keeps the water group peak at a higher energy than the light ion group peak. Since the selected data are all

from the equatorial plane, one constraint keeps the bulk flow component V_z at zero. The cost function is also constrained to use energies only between 5 eV and 27.5 keV as these enveloped the observed water and light ion group distributions. This constraint reduces computational time and reduces the influence of random noise from the highest and lowest ends of the spectra. Uncertainties for each fitted parameter are assigned as outlined by *Press et al.* [1992, section 15.6], where the $\Delta\chi^2$ value at the 90% confidence level is computed and the square root of that multiplied by the appropriate diagonal value in the covariance matrix provides the uncertainty in each parameter fitted.

[16] The forward modeling code will always produce a result; however, the result that gives the minimum cost function may not be physically reasonable. In other cases, a visual comparison of the simulated and real spectra may highlight regions where the code found a poor fit. A manual inspection of moments for each 448 s interval is therefore performed, and results are removed that do not meet all the following requirements:

[17] 1. None of the moments are at the limits set in the constraints (exception for $V_z = 0$).

[18] 2. The cost function is below a critical limit, in this case 5×10^5. This value was obtained from experience after examining the quality of numerous fits.

[19] 3. A full 448 s of data are included, without data gaps.

[20] 4. Within the 448 s interval there is a clear separation between the water and light ion peaks in the measured IMS singles data.

[21] 5. It is assumed that the plasma environment is constant throughout the interval; hence no interchange/dispersion events [*Burch et al.*, 2005; *Hill et al.*, 2005] can be present.

[22] 6. The true peak of the population is clearly inside the field of view of IMS. If either the peak count rate in the measured data is in one of the edge anodes (1 and 8) or the actuator does not sweep past the main beam twice (i.e., completely through it back and forward) then it is assumed that the real peak has not been measured and the interval is unsuitable for moments calculations.

[23] Figure 3 shows an example of observed and simulated spectrograms for one such interval that met all the criteria (the interval between times A and B in Figure 2). The back and forward sweep through the main beam is clearly evident as enhanced count rates. The main beam is sampled in the column marked C, the counts then drop in the next column before returning in the next one. Had just one peak been visible the interval would have been rejected, even though it is possible the actuator really did pass through the peak twice but owing to the telemetry mode the data were averaged to produce a single peak in the data records. Figure 4 is an example field of view plot for the interval between A and B, projecting all 4π steradians of space to a 360° hemisphere fish-eye view, with the coverage of the 8 anodes shown as just a fraction of the total space.

[24] Figure 5 shows the energy distribution of the measured and simulated data for anodes 2, 4 and 6 (colored red, green and blue, respectively) at the time marked as C on Figure 3. The thick lines are the measured IMS singles data, while the thin lines are the simulated ion counts. For each anode the magnitude and location of both the simulated H$^+$
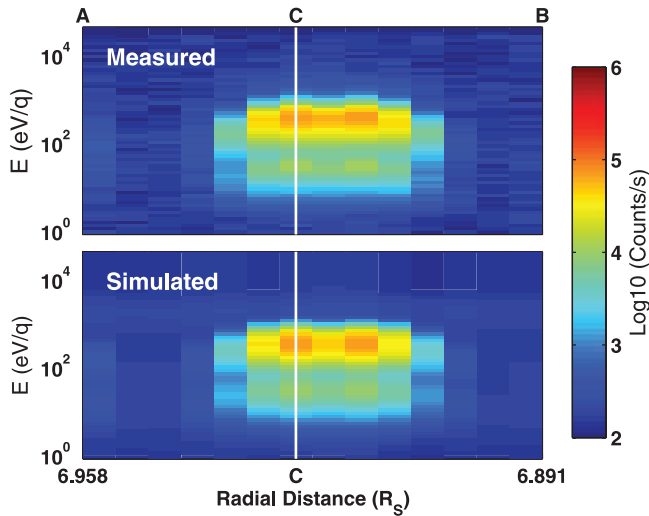
Figure 3. A comparison of (top) measured and (bottom) simulated spectrograms for anode 4 for the interval A-B of Figure 2, for the duration of one moments calculation, 448 s. Clearly, the main features of the measured spectrogram are well represented in the simulated version. A line plot through C is shown in Figure 5.

and W^+ peaks correspond well to the measured data, as does the trough between these peaks. While the fit could be further improved in these three examples, it should be remembered the best fit moments used in this simulated data set apply to all data records within the 448 s interval and not just this slice. Clearly they still provide a satisfactory match to the measured data.

5. Results

[25] After analysis, 150 intervals of 448 s were retained that met all the criteria (their distribution is shown in Figure 1). Examining the locations of these intervals it was found that they were all within ±0.4 degrees latitude of the equator.

[26] Figure 6 shows a plot of the resulting total ion number density $(n^W + n^H)$ against radial distance, along with the fit to the electron density $n_e = 51880 \ (R/R_s)^{-4.1} \ cm^{-3}$ derived by *Persoon et al.* [2006] from Cassini RPWS data between 5 and 8.6 R_s. The two results are in reasonable agreement, and although the RPWS fit is not a perfect match to the IMS density, it is worth noting that it is a comparable match to the RPWS data that were used to derive it, including the largest underestimation around 7 R_S. Carrying out similar power law fits to IMS densities for R < 8.6 R_S gave the forms $(n^W + n^H) = 93520 \ (R/R_s)^{-4.3} \ cm^{-3}$ and $n^W = 113900 \ (R/R_s)^{-4.5} \ cm^{-3}$, with power law exponents similar to that of the RPWS fit. Repeating the power law fit to include all data (R < 11 R_S) gave the form $(n^W + n^H) = 243800 \ (R/R_s)^{-4.8} \ cm^{-3}$ and $n^W = 287200 \ (R/R_s)^{-5.0} \ cm^{-3}$; including the data at larger R has the effect of changing the power term from ~-4 to ~-5.

[27] However, a superior fit to the IMS data is found if one assumes that the density falls exponentially with the square of radial distance, as this follows the trend in the data more closely than a power law. Assuming the form

$n = A \ exp(-B \ (R/R_S)^2)$ where A and B are constants and R is radial distance, the coefficients A and B were found for the three cases of n^W, n^H and $(n^W + n^H)$, including data for the whole range of R investigated in this paper. The coefficients are given in Table 1, and the curve for the total density is overlaid in black on Figure 6.

[28] As expected, the dominant ion was that of the water group. The ratio n^W/n^H is shown in the top of Figure 6 and shows a slight decrease with R. The black line is the n^W/n^H ratio from the model fits provided in Table 1, which similarly produces a decrease with R because of the different values of B in the fit. *Sittler et al.* [2008] inferred 2-D contour plots of density (their Figure 6) based on the SOI results of *Sittler et al.* [2006]. Taking a slice along their 2-D figure at the equator the W^+ 50, 30 and 10 cm^{-3} contours are approximately at 5.4, 6.4 and 7.4 R_S, respectively, whereas the exponential fit above assigns those densities at 5.3, 6.3 and 8.1 R_S, showing reasonable agreement.
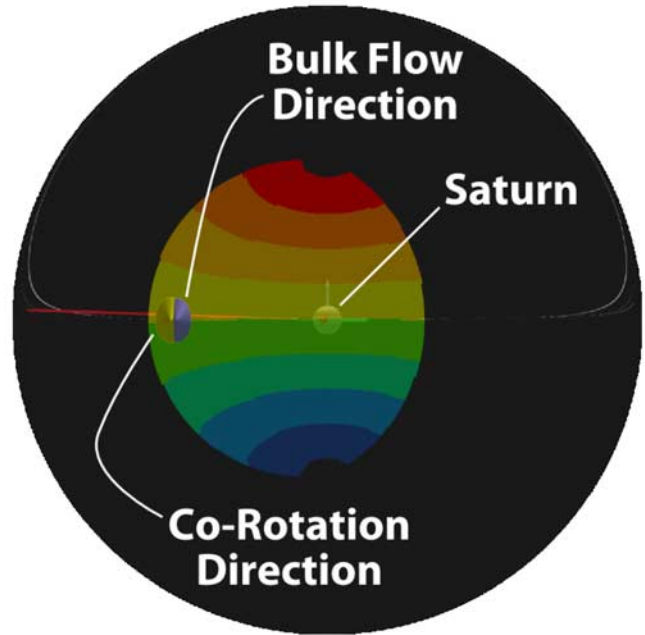

Figure 4. An example of the field of view of CAPS in an arbitrary coordinate system for the interval A-B, highlighting that CAPS cannot view all 4π steradians. This shows all 4π steradians of space around Cassini projected as a 360° hemisphere fish-eye view, along with the field of view of each of the 8 anodes during the interval (each anode has a different color). Two arrow heads can be seen indicating the direction of rigid corotation and the derived velocity direction for this period, falling within the instrument field of view. However, this interval was not included within this study owing to the anodes actuating over fixed pitch angles rather than across them, which was against the data selection criteria. It is included here as the interval A-B provided the clearest data for Figures 2, 3, and 5 among the data surveyed, irrespective of actuation direction, while the total field of view volume is representative of data intervals that were selected for use within this study.
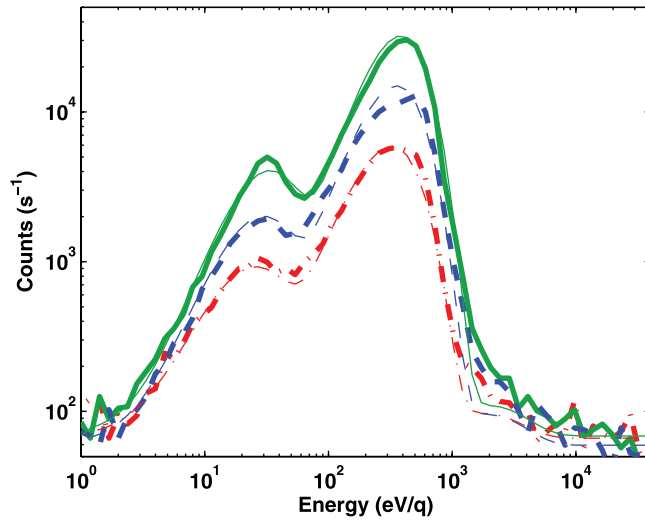
Figure 5. Line plots comparing measured and simulated spectra for one individual IMS sweep, indicated by line C in Figure 3. The thick lines are measured data, while the thin lines are the simulated data. Anodes 2, 4, and 6 are shown and represented by the colors red, green, and blue, respectively.

[29] Figure 7 shows the variation of the perpendicular and parallel temperatures of W^+ with respect to radial distance. At low R, W^+ is clearly anisotropic with $T_\perp/T_\parallel$ ratios of $\sim 3-8$. As R increases the ions become more nearly isotropic, with $T_\parallel$ increasing faster than $T_\perp$.

[30] Around the orbital distance of Dione, $T_\perp$ and $T_\parallel$ for W^+ show local minima in both trajectory segments covering

this region, yet a significant difference in anisotropy between those two passes is observed. These two passes traverse extremely similar local time versus R trajectories, as evidenced in Figure 1, so it is not clear why they are so different. Perhaps this is an indication of temporal variations within the magnetosphere. Nonetheless, all the derived anisotropy values are essentially in the same range, within error, as *Richardson and Sittler* [1990] previously found with Voyager data (their Figure 7).

[31] Figure 8 is the equivalent temperature plot for H^+, again with a local minima in value around the orbital distance of Dione. The temperature anisotropies ($T_\perp/T_\parallel$, Figure 8, bottom) show a scatter without an obvious trend, with a mean value of 2.17 ± 0.42.

[32] These derived temperatures for both W^+ and H^+ are in reasonable agreement with earlier work by *Sittler et al.* [2006], who had examined SOI data utilizing numerical moments techniques and assumed isotropic distributions, all important distinctions from the forward modeled anisotropic distributions from the equator presented here. They were able to fit straight lines to their isotropic temperatures for the region 3.5 to 10 dipole L, represented in Figures 7 and 8 as thin gray lines, of the form $T^H = 2.2*(L/4)^{2.5}$ and $T^W = 35.0*(L/4)^{2.0}$. For the forward modeled results a straight-line fit is insufficient to represent the tick shaped profile with a minimum near Dione's orbit. The total ion density profile during SOI of *Sittler et al.* [2006] (their Figure 14) is of a similar shape to those presented in Figure 6 here but around a factor of ~ 2 lower, likely due to using SOI data which is not on the equator.

[33] *Sittler et al.* [2008] assumed the anisotropies ($T_\perp/T_\parallel$) of W^+ and H^+ were independent of L, and assigned them values of 5 and 2, respectively, the H^+ anisotropy being in
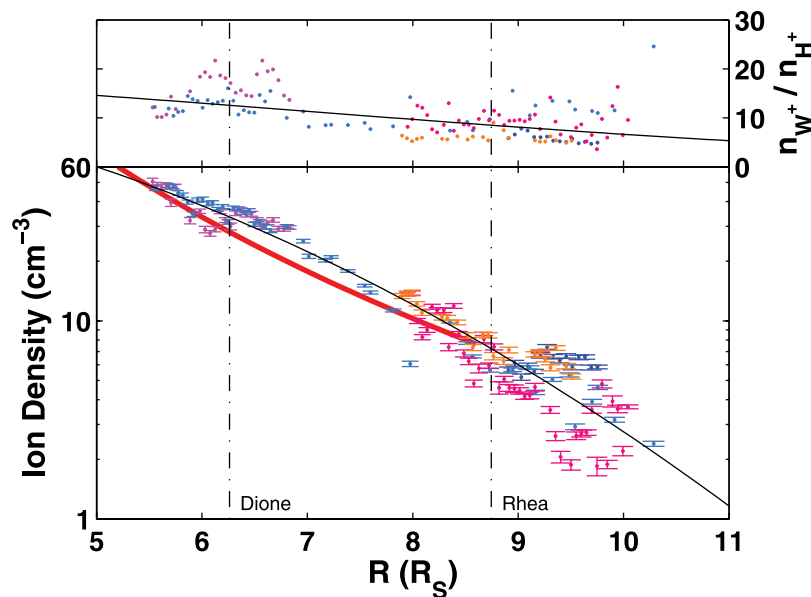

Figure 6. (bottom) Total ion density (the sum of both species) versus radial distance for the moments calculated in this study. The colors of the data points correspond to the orbits shown in Figure 1. For comparison, the thick red line is the electron density modeled by *Persoon et al.* [2006], while the thin black line is the density fit given by Table 1 in this paper for the sum of both species. (top) The ratio of W^+ to H^+ number densities, with the thin line being the ratio found from the density fits for W^+ and H^+ given in Table 1.

Table 1. Coefficients for Fit to Radial Dependence of Density, Assuming the Form n = A exp $(-B (R/R_S)^2)^a$

Ion Species	A (cm^{-3})	B	Coefficient of Determination, R^2
$n^W + n^H$	167.3	0.041	0.933
n^W	161.5	0.042	0.938
n^H	8.3	0.031	0.738

[a]Where n is density in cm^{-3} and R is radial distance.

good agreement with the mean value presented here (2.17 ± 0.42). The derived temperatures anisotropies for W$^+$ generally decrease with R (Figure 7), but if it is assumed there is an independence from L (or R) the mean anisotropy for W$^+$ is 2.91 ± 1.61 which is within a factor of 2 of their assumed value of 5. *Sittler et al.* [2008] later derive W$^+$ anisotropies based on RPWS density scale height measurements and CAPS data (their Figure 11). Considering just the L range examined in this paper their profile is approximately V shaped, with T$_\perp$/T$_\parallel$ dropping almost linearly from ~2.5 to ~1 during 5.5 to 8.5 L, then increases, again approximately linearly (although with greater fluctuations) to ~2 at 10 L. By comparison the forward modeled anisotropy is ~4 at 5.5 R$_S$ with a trend that decreases as R increases with no sign of a turning point, being about ~2 at 8.5 R$_S$.

[34] The derived temperature profiles shown in Figures 7 and 8 do not allow for a simple empirical fit to the data to be made. As such Table 2 lists these derived temperatures and anisotropies for both W$^+$ and H$^+$ ions when binned in to 0.5 R$_S$ intervals in order to aid modelers of Saturn's inner magnetosphere in their work.

[35] Figure 9 shows the derived azimuthal flow component V$_\varphi$ versus radial distance. The plasma is lagging behind rigid corotation by 15–30% over the radial distance investigated, in reasonable agreement with the velocity profile derived by *Mauk et al.* [2005] from Cassini MIMI data during SOI (heavy dashed curve). The values found are greater than those measured by Voyager 1 and Voyager 2 [*Eviatar and Richardson*, 1986], but as with Cassini SOI the Voyager trajectories were off the equator.

[36] The fractional lag behind pure corotation is greatest at distances between 7 and 9 R$_S$ (Figure 9, top). *Saur et al.* [2004] suggest a model that has two local maxima in magnetospheric "conductance" that cause dips in azimuthal velocity at particular radial distances. For Voyager 1 they identified these dips at ~7 and ~10 R$_S$, while for Voyager 2 they identified them at ~7 and ~9 R$_S$, citing seasonal and/or temporal changes in Saturn's magnetosphere as possible reasons for the differences. In our study over 5 different passes it is clear there is an extended dip around 7–9 R$_S$, which within the Saur et al. model would suggest that the two conductance maxima are close together during these intervals. In this study it is not possible to locate a potential second dip in V$_\varphi$ near 10 R$_S$ as there are very few data points in this region. The trajectory with the clearest dip in V$_\varphi$ is from the 24/25 February 2006 trajectory segment where it drops from 70 to 60 km/s over a range of just 0.2 R$_S$, with the dip being centered at ~8.5 R$_S$.

[37] A simple quadratic fit to the forward modeled V$_\varphi$ may be made for the 5.5 to 10 R$_S$ region, the coefficients of which are listed in Table 3, and shown as the thin curve in Figure 9. Variations between different orbits may be linked to different solar wind ram pressures, different planetary
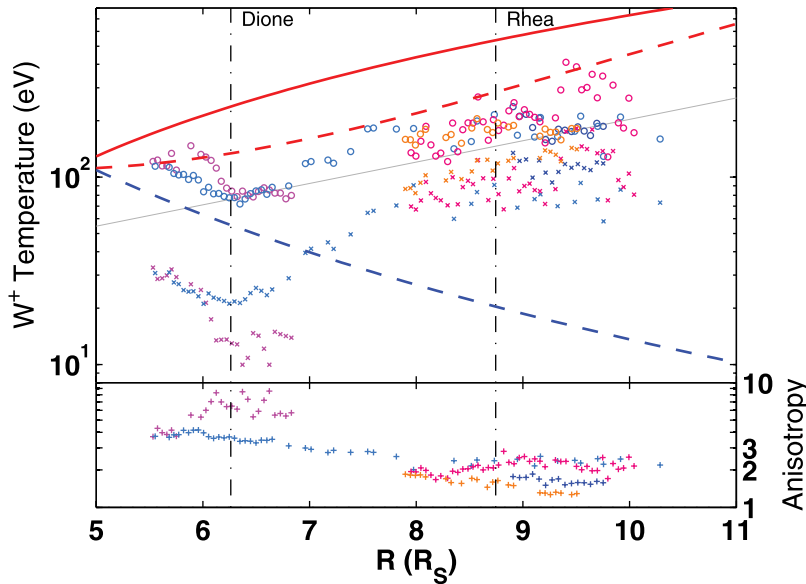

Figure 7. (top) W$^+$ ion temperatures (o = T$_\perp$, x = T$_\parallel$) versus radial distance. The colors of the data points correspond to the orbits shown in Figure 1. The solid red curve shows the value of T$_\perp$ appropriate to local pickup at full corotation (see text). The dashed red curve shows the same thing for local pickup at the observed rotational speed (Figure 9) instead of full corotation. The dashed blue curve shows the result of adiabatic outward transport of an ion picked up at 5 R$_S$. The thin gray line is the isotropic W$^+$ temperature fit from SOI data by *Sittler et al.* [2006]. (bottom) The temperature anisotropy (T$_\perp$/T$_\parallel$) of these ions on the same color scale.

Figure 8. (top) H$^+$ ion temperatures (o = T$_\perp$, x = T$_\parallel$) versus radial distance. The colors of the data points correspond to the orbits shown in Figure 1. The thin gray line is the isotropic H$^+$ temperature fit from SOI data by *Sittler et al.* [2006]. (bottom) The temperature anisotropy (T$_\perp$/T$_\parallel$) of these ions on the same color scale.
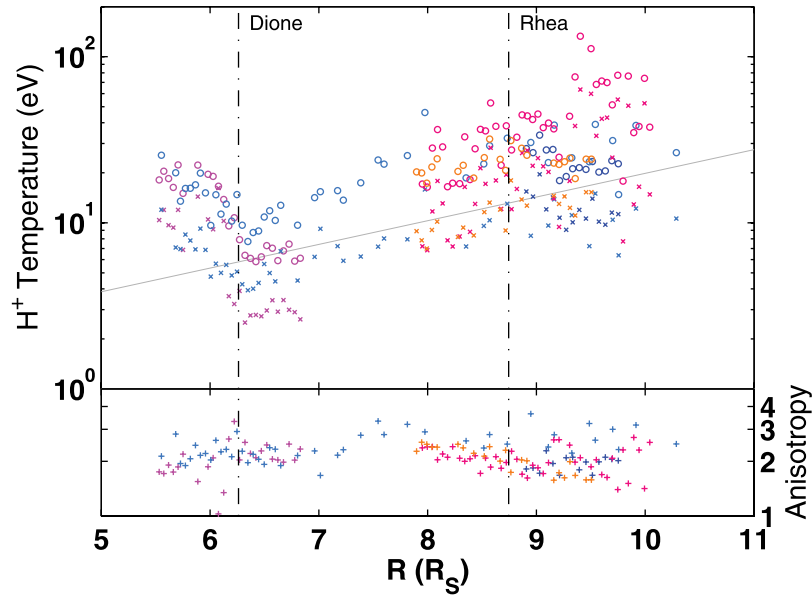
longitudes, or temporal changes within Saturn's magnetosphere. Although several trajectories traverse very similar local times, they cover very different ranges of planetary longitude.

[38] The forward modeled radial flow component V$_\rho$ versus radial distance is shown in Figure 10. The values fluctuate between positive and negative, with an average of 1.1 ± 3.5 km/s, which suggests a small average outflow. The magnitude of V$_\rho$ increases with radial distance, as does the magnitude of **V**. The angular deflection of the bulk flow from the corotation direction, calculated as arctan(V$_\rho$/V$_\varphi$), is shown in the top. The magnitude of the deflection (irrespective of sign) increases with radial distance, and the deflections are within the range -7.5 to $+10$ degrees. This is significant within the context of this study because the IMS singles data used here are only from intervals where the actuator cuts across pitch angle, meaning that any variation in radial flow is identified by comparing data from different anodes only, rather than through actuator motion. Since each anode has a 20 degree width, this situation is less than ideal for finding deflections of only a few degrees, and thus the V$_\rho$ results are the least resolved of the forward modeled moments presented here. *Sittler et al.* [2006] used

a form of numerical integration on Cassini SOI data that assumed isotropy in order to calculate the radial velocity. Their results had a trend that was manually fit to the form $V_\rho = 0.12 \, (R/4)^{5.5}$ (their Figure 10). This gives a very poor fit to the equatorial data shown here (thin line in Figure 10, bottom).

6. Discussion

[39] When Cassini is oriented such that the IMS instrument can observe the main ion distribution, the forward modeling technique has provided an excellent tool with which to examine ion velocity moments. Fitting the measured IMS singles data to just two Maxwellian ion species produces moments that are in reasonable agreement with other independent Cassini instruments, RPWS and MIMI. The forward modeled V$_\varphi$ profile and water group temperature anisotropies generally support results from previous work on Voyager data. The water group was found to be the dominant ion group in the range 5.5 to 10 R$_S$; however, its dominance slightly decreases with radial distance. The ion bulk velocity was found to lag pure corotation, with a maximum in fractional lag around 8 R$_S$.

Table 2. Derived Temperature Data Binned to 0.5 R$_S$ Intervals, Each Bin Centered on the Given R

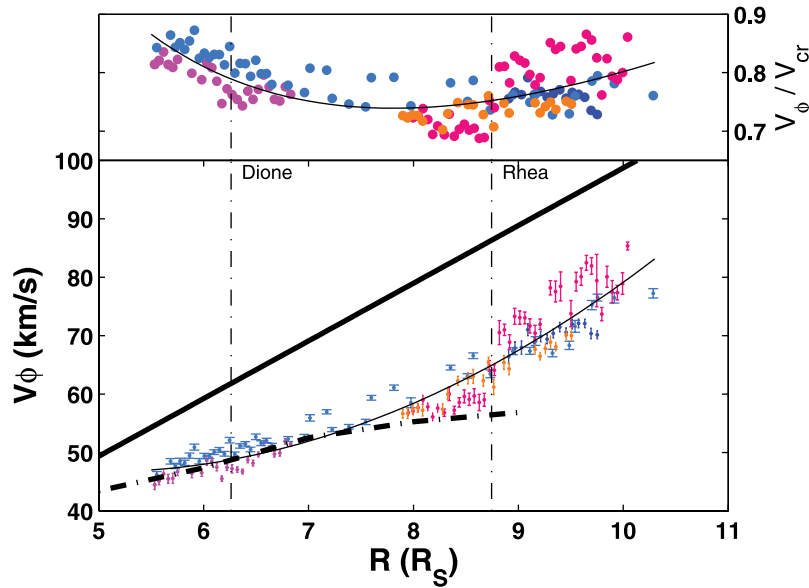| R (R$_S$)	W$^+$ T$_\perp$ (eV)	W$^+$ T$_\parallel$ (eV)	W$^+$ T$_\perp$/T$_\parallel$	H$^+$ T$_\perp$ (eV)	H$^+$ T$_\parallel$ (eV)	H$^+$ T$_\perp$/T$_\parallel$
5.5	117.5	30.2	3.89	19.3	9.9	1.98
6.0	101.4	22.0	4.83	15.0	7.6	2.16
6.5	81.9	17.5	5.23	8.2	3.8	2.17
7.0	103.9	32.0	3.68	11.5	5.5	2.13
7.5	166.9	60.1	2.78	21.3	7.2	2.97
8.0	156.9	82.4	1.91	24.0	9.9	2.44
8.5	180.1	94.4	1.93	27.9	13.1	2.19
9.0	196.9	101.4	2.02	31.6	16.0	2.06
9.5	225.9	122.4	1.86	42.5	22.2	2.02
10.0	197.5	94.0	2.10	39.5	20.5	2.25

Figure 9. (bottom) The bulk flow V_φ component versus radial distance. The colors of the data points correspond to the orbits shown in Figure 1. The thick straight line shows the rigid corotation velocity; the thin line is the quadratic fit given in Table 3. The heavy dashed line shows the MIMI SOI velocity profile for comparison [*Mauk et al.*, 2005]. (top) The same data, and the quadratic fit (black line), as a fraction of the corotation velocity, highlighting the maximum in fractional corotation lag near 8 R_S.

Water group ion temperatures are clearly anisotropic, with $T_\perp > T_\parallel$. They become more nearly isotropic as radial distance increases but are still not isotropic by 10 R_S.

[40] The various ion velocity moments follow consistent patterns of radial variation when data from the five orbits are combined, although there are obvious differences from one orbit to another. These differences may result from solar wind pressure variations, longitudinal variations, or true time variations within the inner magnetosphere. Further study is clearly needed to sort out the causes of these orbit-to-orbit variations.

[41] The radial variations of the ion velocity moments contain several clues to the location(s) of the important plasma source(s):

[42] 1. The observed density profile (Figure 6) suggests a dominant plasma source inside of 5.5 R_S (the inner limit of our study). In the absence of sources or losses, the adiabatic radial transport profile would be $n \propto R^{-m}$ with $3 < m < 4$. (The limit $m = 4$ corresponds to conservation of flux tube content with isotropic plasma filling the flux tube, while the limit $m = 3$ corresponds to conservation of flux tube content with a constant vertical scale height. The $m = 3$ limit is more appropriate here, both because of the observed ion anisotropy $T_\perp > T_\parallel$, and because of centrifugal confinement [*Hill and Michel*, 1976].) The fact that the observed radial profile is $n \propto R^{-m}$ with $m > 4$ indicates that the plasma is either undergoing net outward radial transport and experiencing a net loss process during the transport, or vice versa, undergoing net inward radial transport and experiencing a net source process during the transport. The distinction between these two possibilities relies, among other independent considerations, on clue 2. In addition to the global-scale radial profile, there is a suggestion of a localized secondary source near the orbit of Dione in the

mauve data points in Figure 6 (the points restricted to 5.5 $R_S <$ $R < 6.9$ R_S).

[43] 2. The observed radial variation of W^+ temperature anisotropy (Figure 7) is also consistent with an ion source at $R \leq 5.5$ R_S, but clearly inconsistent with an ion source much farther out. Fresh near-equatorial pickup ions (whether from charge exchange or from photo- or electron-impact ionization) are created with $T_\perp \gg T_\parallel$. This extreme anisotropy is relaxed with time (owing, for example, to scattering by electromagnetic ion cyclotron (EMIC) waves excited by the anisotropy) as the ions are transported (either inward or outward) away from their source. EMIC waves are observed by the Cassini magnetometer in the inner magnetosphere, with peak amplitudes at $R < 5$ R_S [*Leisner et al.*, 2006]. The fact that the observed ion temperature anisotropy is a generally decreasing function of radial distance provides further evidence for a source inside the minimum distance (5.5 R_S) covered by our study. Again, the more localized perturbations near the orbit of Dione on the mauve orbit are worthy of further study.

[44] 3. The variation of W^+ $T_\perp$ itself with radial distance is worthy of note. Figure 7 includes three reference curves: the solid red curve shows the value of $T_\perp$ that would result if the ions were picked up locally with thermal speed equal to the full corotation speed less the Kepler orbital speed; the dashed red curve shows the same thing but using the observed rotational speed (the polynomial fit to the data

Table 3. Coefficients Found to Fit the Measured V_φ, Assuming the Form $V_\varphi = A\ (R/R_S)^2 + B(R/R_S) + C$

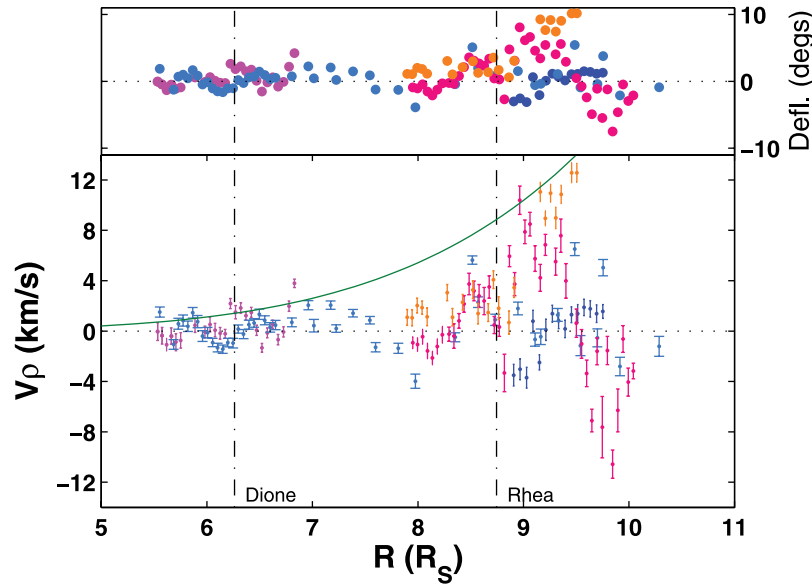| A (km/s)	B (km/s)	C (km/s)	Coefficient of Determination, R^2
1.29	−12.82	78.56	0.933

Figure 10. (bottom) The bulk flow V_ρ component versus radial distance. The colors of the data points correspond to the orbits shown in Figure 1. The solid green line shows for comparison the radial velocity model of *Sittler et al.* [2006]. (top) The angular deflection from the corotation direction, given by $\arctan(V_\rho/V_\varphi)$.

in Figure 9) instead of full corotation; the dashed blue curve shows for comparison the result of outward transport in a dipole field conserving the first adiabatic invariant ($T_\perp \propto L^{-3}$) for ions picked up at 5 R_S. As expected, all data points fall between the dashed red and dashed blue curves, with the exception of a few points that are only slightly above the dashed red curve. However, if ions in this radial range are transported outward from a source within 5.5 R_S, as suggested above, it is clear that the outward transport is not adiabatic. An analogous phenomenon is well known at Jupiter [e.g., *Belcher*, 1983; *Hill et al.*, 1983] but not yet fully explained. A plausible explanation, at least in the Saturn context, is an extended region of charge exchange reactions between transporting plasma and ambient neutral gas. Charge exchange removes an ion from the ambient population (presumably somewhere between the dashed red and blue curves), and replaces it with an ion on the dashed red curve, thus biasing the ambient population to favor the dashed red curve rather than the dashed blue curve, while still remaining somewhere in between. The implication would be that charge exchange (and/or new ionization) remains significant out to $L \sim 10$, because the W^+ $T_\perp$ data are closer to the dashed red curve than the dashed blue curve.

[45]   4. The observed corotation-lag profile (Figure 9) also contains information about the location(s) of plasma source(s). Extracting this information, however, requires new theoretical modeling that is beyond the scope of this paper. There are four things that can cause a significant corotation lag: (1) external (e.g., solar wind) influences, (2) local plasma production, (3) momentum-exchange collisions between ions and neutrals, including but not necessarily limited to charge exchange collisions, and (4) radial transport of plasma produced elsewhere in the magnetosphere. Effect 1 is safely neglected in the inner magnetospheres of both Jupiter and Saturn, insofar as the corotation lag is concerned [e.g., *Hill et*

al., 1983, and references therein]. Effects 2–4 are not. Effects 2 and 3 have similar influences on the corotation-lag profile, and are often lumped together under the term "mass loading." Effect 4 has a different influence, and may be called "mass transport." The mass loading and mass transport effects are well separated spatially in the case of Jupiter, where the mass loading effect is confined to the near vicinity of the Io plasma torus ($R \sim 6$ R_J) and the mass transport effect only becomes important farther out ($R > \sim 10$ R_J). These two regimes have been studied separately by *Pontius and Hill* [1982] and by *Hill* [1979], respectively, for Jupiter. Saturn presents a new problem, compared to Jupiter, in that the mass loading region significantly overlaps the mass transport region, so that the two effects are not mathematically separable. A further complication is that the rate of charge exchange is expected to exceed the rate of new ionization in Saturn's inner magnetosphere [e.g., *Tokar et al.*, 2006; *Johnson et al.*, 2006]. Charge exchange contributes to the local corotation lag but not to the rate of outward plasma transport. Preliminary application of a more general theoretical analysis (D. H. Pontius and T. W. Hill, manuscript in preparation, 2008) to the experimental results reported here supports the conclusion that an important fraction of the plasma mass loading occurs inside the 5.5 R_S inner boundary of the present study. This conclusion is consistent with the observations by CAPS of ion pickup distributions inside 5.5 R_S [*Tokar et al.*, 2008].

[46]   Assuming inductive electric fields to be negligible, the radial flow component V_ρ (Figure 10) must average to zero when averaged over time and over longitude (or local time). The observed radial components (Figure 10) are consistent with this expectation. The magnitudes $|V_\rho|$ are small compared to V_φ. The average V_ρ component is slightly positive, as noted above. Recall, however, that interchange/dispersion events were explicitly excluded from our data set, thus excluding narrow longitudinal sectors of

fast inward flow [*Burch et al.*, 2005; *Hill et al.*, 2005; *Chen and Hill*, 2008]. Further study is needed to test the hypothesis that fast inward flow is associated with narrow sectors of hot tenuous plasma, while slower outward flow is associated with broader sectors of cooler, denser, plasma of the type analyzed here.

References

Belcher, J. W. (1983), The low-energy plasma in the Jovian magnetosphere, in *Physics of the Jovian Magnetosphere*, edited by A. J. Dessler, chap. 3, pp. 68–105, Cambridge Univ. Press, Cambridge, U. K.

Brent, R. P. (1973), *Algorithms for Function Minimization Without Derivatives*, Prentice-Hall, Englewood Cliffs, N. J.

Burch, J. L., J. Goldstein, T. W. Hill, D. T. Young, F. J. Crary, A. J. Coates, N. André, W. S. Kurth, and E. C. Sittler Jr. (2005), Properties of local plasma injections in Saturn's magnetosphere, *Geophys. Res. Lett.*, *32*, L14S02, doi:10.1029/2005GL022611.

Chen, Y., and T. W. Hill (2008), Statistical analysis of injection/dispersion events in Saturn's inner magnetosphere, *J. Geophys. Res.*, *113*, A07215, doi:10.1029/2008JA013166.

Eviatar, A., and J. Richardson (1986), Corotation of the Kronian magnetosphere, *J. Geophys. Res.*, *91*, 3299, doi:10.1029/JA091iA03p03299.

Hill, T. W. (1979), Inertial limit on corotation, *J. Geophys. Res.*, *84*, 6554, doi:10.1029/JA084iA11p06554.

Hill, T. W., and F. C. Michel (1976), Heavy ions from the Galilean satellites and the centrifugal distortion of the Jovian magnetosphere, *J. Geophys. Res.*, *81*, 4561, doi:10.1029/JA081i025p04561.

Hill, T. W., A. J. Dessler, and C. K. Goertz (1983), Magnetospheric models, in *Physics of the Jovian Magnetosphere*, edited by A. J. Dessler, chap. 10, pp. 353–394, Cambridge Univ. Press, Cambridge, U. K.

Hill, T. W., A. M. Rymer, J. L. Burch, F. J. Crary, D. T. Young, M. F. Thomsen, D. Delapp, N. André, A. J. Coates, and G. R. Lewis (2005), Evidence for rotationally driven plasma transport in Saturn's magnetosphere, *Geophys. Res. Lett.*, *32*, L14S10, doi:10.1029/2005GL022620.

Ingber, L. (1993a), Adaptive Simulated Annealing (ASA), global optimization C-code, Caltech Alumni Assoc, Pasadena, Calif.

Ingber, L. (1993b), Simulated Annealing: Practice versus Theory, *Math. Comput. Model.*, *18*(11), 29–57, doi:10.1016/0895-7177(93)90204-C.

Ingber, L. (1996), Adaptive simulated annealing (ASA): Lessons learned, *Control Cybern.*, *25*(1), 33–54.

Johnson, R. E., H. T. Smith, O. J. Ticker, M. Liu, M. H. Burger, E. C. Sittler, and R. L. Tokar (2006), The Enceladus and OH tori at Saturn, *Astrophys. J.*, *644*, L137–L139, doi:10.1086/505750.

Leisner, J. S., C. T. Russell, M. K. Dougherty, X. Blanco-Cano, R. J. Strangeway, and C. Bertucci (2006), Ion cyclotron waves in Saturn's E ring: Initial Cassini observations, *Geophys. Res. Lett.*, *33*, L11101, doi:10.1029/2005GL024875.

Mauk, B. H., et al. (2005), Energetic particle injections in Saturn's magnetosphere, *Geophys. Res. Lett.*, *32*, L14S05, doi:10.1029/2005GL022485.

Persoon, A. M., D. A. Gurnett, W. S. Kurth, and J. B. Groene (2006), A simple scale height model of the electron density in Saturn's plasma disk, *Geophys. Res. Lett.*, *33*, L18106, doi:10.1029/2006GL027090.

Pontius, D. H. Jr., and T. W. Hill (1982), Departure from corotation of the Io plasma torus: Local plasma production, *Geophys. Res. Lett.*, *9*, 1321, doi:10.1029/GL009i012p01321.

Powell, M. J. D. (1964), An efficient method for finding the minimum of a function in several variables without calculating derivatives, *Comput. J.*, *7*, 155–162, doi:10.1093/comjnl/7.2.155.

Press, W. H., S. A. Teukolsky, W. T. Vetterling, and B. P. Flannery (1992), *Numerical Recipes in C: The Art of Scientific Computing*, 2nd ed., Cambridge Univ. Press, Cambridge, U. K.

Richardson, J. D. (1986), Thermal ions at Saturn: Plasma parameters and implications, *J. Geophys. Res.*, *91*, 1381, doi:10.1029/JA091iA02p01381.

Richardson, J. D., and E. C. Sittler Jr. (1990), A plasma density model for Saturn based on Voyager observations, *J. Geophys. Res.*, *95*, 12,019, doi:10.1029/JA095iA08p12019.

Saur, J., B. H. Mauk, A. Kaßner, and F. M. Neubauer (2004), A model for the azimuthal plasma velocity in Saturn's magnetosphere, *J. Geophys. Res.*, *109*, A05217, doi:10.1029/2003JA010207.

Sittler, E. C., Jr., et al. (2005), Preliminary results on Saturn's inner plasmasphere as observed by Cassini: Comparison with Voyager, *Geophys. Res. Lett.*, *32*, L14S07, doi:10.1029/2005GL022653.

Sittler, E. C., Jr., et al. (2006), Cassini observations of Saturn's inner plasmasphere: Saturn orbit insertion results, *Planet. Space Sci.*, *54*, 1197–1210, doi:10.1016/j.pss.2006.05.038.

Sittler, E. C., Jr., et al. (2008), Ion and neutral sources and sinks within Saturn's inner magnetosphere: Cassini results, *Planet. Space Sci.*, *56*, 3–18, doi:10.1016/j.pss.2007.06.006.

Thomsen, M. F., and D. M. Delapp (2005), Numerical moments computation for CAPS/IMS, *LA-UR-05-1542*, Los Alamos Natl. Lab., Los Alamos, N. M.

Tokar, R. L., et al. (2005), Cassini observations of the thermal plasma in the vicinity of Saturn's main rings and the F and G rings, *Geophys. Res. Lett.*, *32*, L14S04, doi:10.1029/2005GL022690.

Tokar, R. L., et al. (2006), The interaction of the atmosphere of Enceladus with Saturn's plasma, *Science*, *311*(5766), 1409–1412, doi:10.1126/science.1121061.

Tokar, R. L., et al. (2008), Cassini detection of water-group pick-up ions in the Enceladus torus, *Geophys. Res. Lett.*, *35*, L14202, doi:10.1029/2008GL034749.

Wolfe, J. H., J. D. Mihalov, H. R. Collard, D. D. McKibbin, L. A. Frank, and D. S. Intriligator (1980), Preliminary results on the plasma environment of Saturn from the Pioneer 11 plasma analyzer experiment, *Science*, *207*, 403, doi:10.1126/science.207.4429.403.

Young, D. T., et al. (2004), Cassini Plasma Spectrometer Investigation, *Space Sci. Rev.*, *114*, 1–112, doi:10.1007/s11214-004-1406-4.

Young, D. T., et al. (2005), Composition and dynamics of plasma in Saturn's magnetosphere, *Science*, *307*, 1262–1266, doi:10.1126/science.1106151.

————————

M. G. Henderson, M. F. Thomsen, R. L. Tokar, and R. J. Wilson, ISR-1, Space and Atmospheric Sciences Group, LANL, P.O. Box 1663, MS D466, Los Alamos, NM 87545-0000, USA. (rjw@lanl.gov)

T. W. Hill, Department of Physics and Astronomy, Rice University, Houston, TX 77251, USA.

D. H. Pontius Jr., Physics Department, Birmingham-Southern College, Birmingham, AL 35254, USA.